npj | 2D Materials and Applications

www.nature.com/npj2dmaterials

ARTICLE OPEN

Check for updates

Quantifying photoinduced carriers transport in exciton–polariton coupling of MoS_2 monolayers

Min-Wen Yu[1,2], Satoshi Ishii[2]✉, Shisheng Li[2], Ji-Ren Ku[3], Jhen-Hong Yang[4], Kuan-Lin Su[3], Takaaki Taniguchi[2], Tadaaki Nagao[2,5] and Kuo-Ping Chen[3]✉

Exciton–polariton coupling between transition metal dichalcogenide (TMD) monolayer and plasmonic nanostructures generates additional states that are rich in physics, gaining significant attention in recent years. In exciton–polariton coupling, the understanding of electronic-energy exchange in Rabi splitting is critical. The typical structures that have been adopted to study the coupling are "TMD monolayers embedded in a metallic-nanoparticle-on-mirror (NPoM) system." However, the exciton orientations are not parallel to the induced dipole direction of the NPoM system, which leads to inefficient coupling. Our proposed one-dimensional plasmonic nanogrooves (NGs) can align the MoS_2 monolayers' exciton orientation and plasmon polaritons in parallel, which addresses the aforementioned issue. In addition, we clearly reveal the maximum surface potential (SP) change on intermediate coupled sample by the photo-excitation caused by the carrier rearrangement. As a result, a significant Rabi splitting (65 meV) at room temperature is demonstrated. Furthermore, we attribute the photoluminescence enhancement to the parallel exciton–polariton interactions.

npj 2D Materials and Applications (2021)5:47 ; https://doi.org/10.1038/s41699-021-00227-y

INTRODUCTION

Strong light–matter interactions exhibit many compelling features, owing to their potential applications in low-threshold lasing[1,2], Bose–Einstein condensate[3,4], and superfluidity[5,6]. These approaches are generally employed using a single emitter and resonant cavity. Furthermore, a strong coupling occurs when the energy-exchange rate exceeds both the emitter scattering rate γ and cavity dissipation rate κ. Upon achieving a strong-coupling regime, a new hybrid eigenstate is formed because of the energy-difference-induced splitting of two polaritonic states. This phenomenon is known as vacuum Rabi splitting. To achieve a strong-coupling regime, the coupling strength g should be greater than $(\gamma, \kappa)/2$[7]. In addition, the intermediate coupling regime is $\gamma > 2g > \kappa$, which has caught some attention lately[8,9]. Therefore, selecting an appropriate emitter and cavity is crucial in such hybrid systems. Thus far, several strong-coupling systems have been demonstrated with dye molecules[10–12] or quantum dots[13–15] as emitters; these conventional platforms have high Rabi splitting energies. Additionally, dye molecules can be easily photo-bleached, and quantum dots are prone to oxidization and agglomeration, both of which hinder their further applications.

Two-dimensional (2D) transition metal dichalcogenide (TMD) semiconductors with structures MX_2, where M is Mo or W and X is S, Se, or Te, have introduced many possibilities in photonics because of their remarkable optical and electronic properties. When the layer number of TMDs is reduced to monolayers, a transition from indirect to direct bandgap semiconductor occurs[16,17]. TMD monolayers have generated significant interest because their excitons can operate in the visible to near-IR regions. Additionally, the excitons are stable at room temperature. Importantly, the exciton binding energies of TMD monolayers (e.g., 240 meV[18] for MoS_2, and 700 meV[19] for WS_2) are significantly higher than γ ($\gamma \sim k_BT = 26$ meV) at room temperature. Because of the above-mentioned advantages, TMDs are appropriate emitters for developing strong-coupling systems.

Additionally, the cavity dissipation rate is critical for the coupling strength. To achieve energy-exchange cycle between the cavities and emitters, a low cavity dissipation rate is required; the rate is inversely proportional to the quality factor Q, i.e., $\kappa \propto 1/Q$. Various types of cavities such as photonic-crystal cavities[20], microcavities[21], and Fabry−Pérot cavities[22] were developed to facilitate strong coupling in TMDs. Because the coupling strength varies as $g \propto \sqrt{1/V}$, where V denotes the effective cavity mode volume[11]; a significantly small cavity mode volume and high-Q resonator are favorable. Accordingly, plasmonic cavities are desirable because of their deep-subwavelength mode volumes. Many recent reports have adopted exciton–plasmon coupling systems that have the metallic-nanoparticle-on-mirror (NPoM) structure, in which TMDs are placed between the metal nanoparticles and mirror[9,23,24]. When an NPoM system is optically illuminated, the gap plasmon mode provides significant electric-field confinement and ultra-small mode volume[11]. However, the strong localized field in NPoM systems is primarily out-of-plane and cannot satisfactorily couple with the in-plane exciton dipole of TMDs[23,25]. Therefore, we propose Au nanogroove (NG) arrays, on the top of which we place MoS_2 monolayers; the strongly localized electric field of Au NGs is parallel to the in-plane exciton dipole of MoS_2 monolayers.

Such exciton–polariton coupling systems with high splitting energy result in a significant reconstruction of the energy levels of the system. To explore the electronic-energy transfer in exciton–polariton coupling systems, the surface potential (SP)

[1]College of Photonics, National Chiao Tung University and National Yang Ming Chiao Tung University, Tainan 71150, Taiwan. [2]International Center for Materials Nanoarchitectonics (MANA), National Institute for Materials Science (NIMS), Tsukuba, Ibaraki 305-0044, Japan. [3]Institute of Imaging and Biomedical Photonic, College of Photonics, National Chiao Tung University and National Yang Ming Chiao Tung University, Tainan 71150, Taiwan. [4]Institute of Photonic System, College of Photonics, National Chiao Tung University and National Yang Ming Chiao Tung University, Tainan 71150, Taiwan. [5]Department of Condensed Matter Physics, Graduate School of Science, Hokkaido University, Sapporo, Hokkaido 060-0810, Japan. ✉email: sishii@nims.go.jp; kpchen@nctu.edu.tw

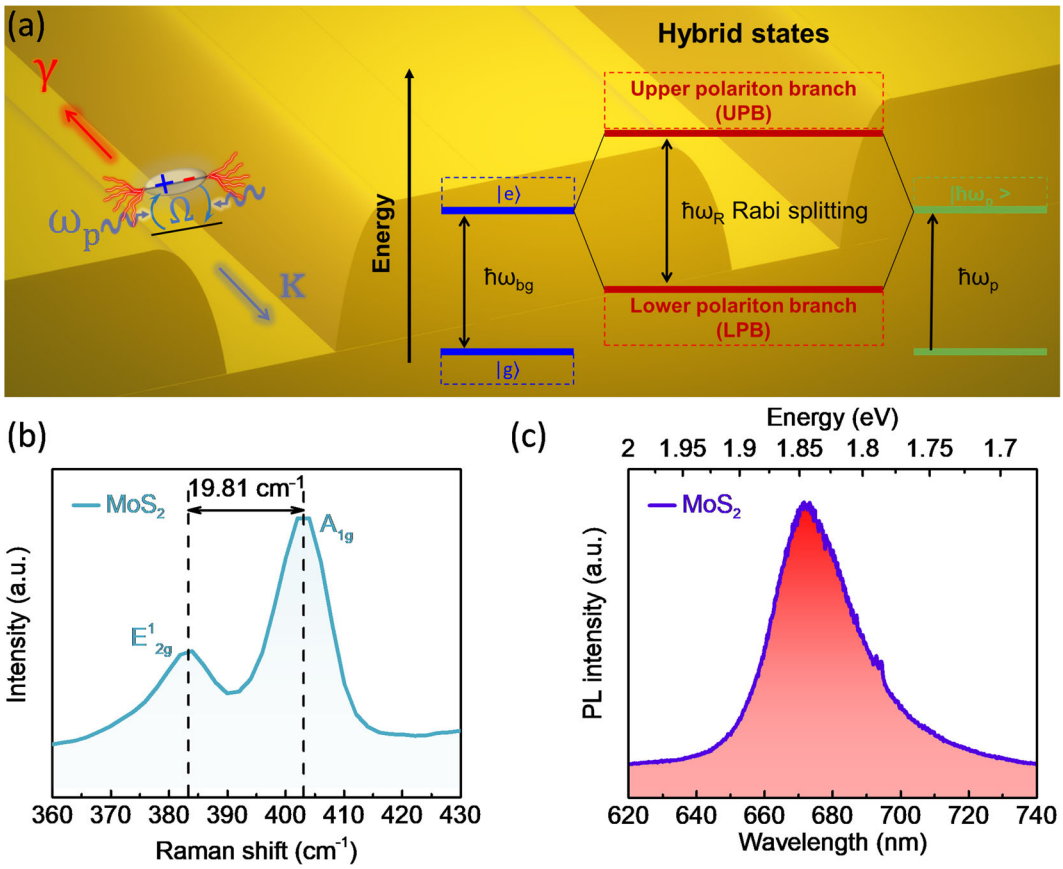

Fig. 1 Rabi splitting and optical characterization of MoS_2. a Exciton–polariton coupling system between a plasmonic cavity with a resonant ω_p and TMD excitons. In this system, the parameters that determine the coupling strength are the energy-exchange rate Ω, cavity loss rate γ, and emitter loss rate κ. The right panel depicts the energy diagram of the strong coupling of the 2D TMD semiconductor with a direct bandgap $\hbar\omega_{bg}$ between the ground state $|g\rangle$ and excited state $|e\rangle$ coupled to the plasmonic-cavity mode $\hbar\omega_p$. The coherent coupling forms a hybrid state with UPB and LPB separated by Rabi splitting energy $\hbar\omega_R$. **b** The Raman spectra of the MoS_2 monolayers after being transferred on the Au film. The frequency difference between the E^1_{2g} and A_{1g} modes is 19.81 cm^{-1}, which indicates monolayers. **c** PL spectra of the MoS_2 monolayers.

change is a crucial evidence. It has been reported[26] that the WF changes the organic material-cavity strong-coupling system. The highest occupied-orbital–lowest-unoccupied-orbital transition in a photochromic spiropyran-doped polymer results in the electronic-energy transfer owing to strong coupling. However, the strong coupling can occur in the absence of light and exchange the coherent energy as mentioned above. The photo-excited bandgap of MoS_2 can excite carriers and induce the electric field of Au NG which cause carrier rearrangement in the exciton–polariton coupling system[27]. The coherent energy exchange between excitons and plasmons in the strong-coupling regime and intermediate coupling can promote charge transfer which has been discussed using far-field pump-probe measurements[27,28]. However, far-field pump-probe measurements cannot provide the evidence of couplings in the nanoscale. By using Kelvin probe force microscopy (KPFM) equipped with a light source, one can calculate the photoinduced SP change of the sample by measuring the surface potential difference (SPD) between the scanning probe and samples at the nanoscale.

In this study, we propose 1D plasmonic NG arrays and incorporate them with 2D MoS_2, which demonstrates a significant Rabi splitting (65 meV) at room temperature. The electric-field distribution clearly reveals the coupling between the NG plasmonic mode and exciton mode. Additionally, the photo-excited carrier transfer from MoS_2 can be facilitated by coherent energy exchange, and the parallel exciton–polariton enhanced the interaction that revealed in the SP change. Many instances of photoluminescence (PL) intensity enhancement were observed. Our findings are important basis to further study the TMD–plasmon coupling.

RESULTS AND DISCUSSION

Strong coupling in MoS_2 monolayers on 1D plasmonic NGs

Figure 1a depicts a two-level system with the ground state ($|g\rangle$) and excited state ($|e\rangle$) separated by $\hbar\omega_{bg}$, which denotes the coupling of a 2D material exciton with an NG cavity. When the energy-exchange rate Ω is higher than the decay rate (γ, κ) of this system, two polaritonic states (upper polariton branch (UPB) and lower polariton branch (LPB)) are formed, which are separated by Rabi splitting. In this study, wafer-scale MoS_2 monolayers were grown using the vapor–liquid–solid method[29,30]. The characteristics of the MoS_2 monolayers were confirmed via Raman-spectroscopy measurements, as depicted in Fig. 1a. As previously reported[31–33], the layer number can be identified by the frequency difference between the E^1_{2g} and A_{1g} modes. Figure 1c depicts the PL spectra of the MoS_2 monolayers excited using a 532 nm continuum-wave (CW) laser, which shows exciton emission at 675 nm (1.84 eV).

To characterize exciton–polariton coupling features, we employed Au NG arrays as optical cavities and transferred the MoS_2 monolayers on their top, as depicted in Fig. 2a. Such plasmonic nanostructures of surface plasmon resonances (SPRs) can be controlled by adjusting the geometry size, and the degree

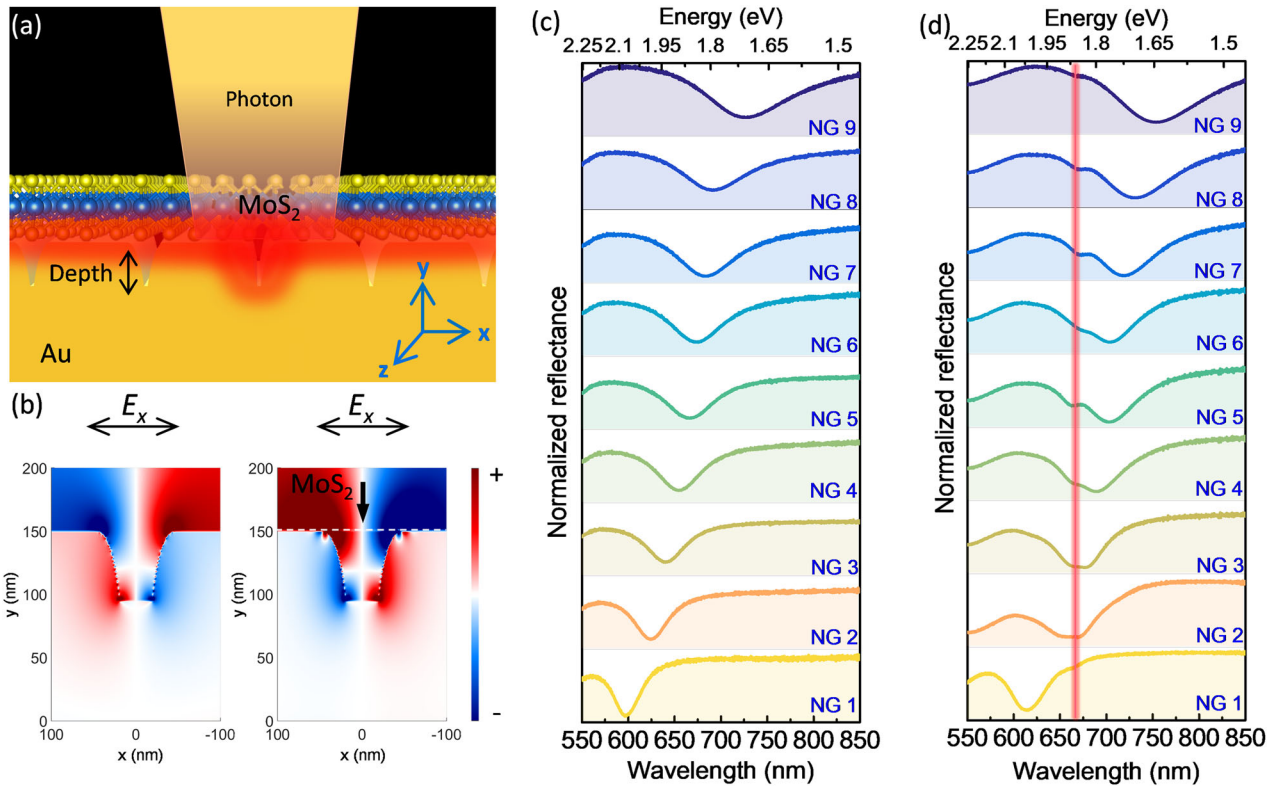

Fig. 2 Features of plexciton system in individual Au NG array. a Au NGs load MoS_2 monolayers on their top. **b** The simulated electric-field distributions of the plasmon-coupled mode of Au NGs (left panel) and loading monolayers MoS_2 (white dashed line) on top (right panel). The incident light is polarized along the *x*-axis. The reflectance spectra of: **c** the Au NGs having various depths, and **d** the Au NGs upon integrating MoS_2 on their top.

of enhancement can also be utilized to study the strong coupling. Au NGs[34,35] generate a strongly local field, which is dominantly in plane; in this field, effective coupling occurs between the NGs and MoS_2 (see Fig. 2b). The NGs were fabricated via focused-ion-beam milling on a 150-nm-thick Au film (Supplementary Fig. 1). Their SPR wavelength can be easily tuned by precisely controlling the NG depth, allowing the adjustment of the SPR wavelength to match the exciton energy of the MoS_2 monolayers. Figure 2c depicts a single-plasmonic mode with individual NGs of various depths which are in the range of 55–105 nm. After integrating the MoS_2 monolayers, a splitting between exciton–plasmon polariton (or plexcitons) was observed in the reflectance spectra (see Fig. 2d). The simulated spectra depicted in Supplementary Fig. 2 was obtained by varying the depth of NG.

In order to determine whether this hybrid system is strongly coupled, we adopted a classical model that predicts UPB and LPB in agreement with the quantum-mechanical Jaynes–Cummings model as[8,11,23]

$$E_{\pm} = \frac{1}{2}\left(E_{\mathrm{p}} + E_0\right) \pm \frac{1}{2}\sqrt{g^2 + \delta^2}, \tag{1}$$

where $E_{\pm}$ represents UPB (+) and LPB (–), as depicted in Fig. 3a; E_{p} and E_0 denote the energy of the pure plasmon-cavity mode and MoS_2 exciton energy, respectively; and $\delta = E_{\mathrm{p}} - E_0$ denotes the detuning energy between plasmon and exciton. Although the thickness of each MoS_2 monolayer is approximately 0.6 nm, the SPRs are sensitive to the change in the surrounding refractive index. Therefore, we red-shifted approximately 26 nm from Fig. 2c, d without considering the coupling effect to obtain a more accurate fitting curve. The coupling strength, as a function of cavity and exciton, can be described as[8,11,23,24]

$$g = \mu_{\mathrm{e}}\sqrt{\frac{4\pi\hbar Nc}{\lambda\varepsilon_0 V}}, \tag{2}$$

where μ_{e}, N, and V denote the exciton-transition dipole moment, number of excitons coupled to the cavity, and mode volume of the cavity, respectively. The intermediate coupling regime was observed with the Rabi splitting energy of 65 meV which is comparable with the excitonic linewidth but smaller than the plasmon linewidth[8,9]. By simulating the 2D contour plot depicted in Fig. 3b, an anticrossing behavior was observed. To numerically understand the MoS_2/NG coupling system, we used a commercial finite-difference time-domain (FDTD) software program (Lumerical) to calculate the Purcell factor $\boldsymbol{F_p} = \frac{3}{4\pi^2}\left(\frac{\lambda_0}{\boldsymbol{n}}\right)^3\frac{\boldsymbol{Q}}{\boldsymbol{V}}$, which describes the enhancement of the spontaneous emission rates of atoms when they integrate into a cavity. In our Au NG nanocavities, $\boldsymbol{F_p} \approx 4.03 \times 10^4$, in which the effective mode volume was calculated to be 78 nm^3 (Supplementary Fig. 3). Moreover, we have listed the strong coupling in TMDs from recent works in Supplementary Table 1. To the best of our knowledge, we have observed the largest Rabi splitting among all the works on MoS_2 at room temperature, and the splitting is even comparable to that at the low temperature of 77 K[36]. The large Rabi splitting is attributed to 1D plasmonic NGs, which can excite plasmonic mode parallel to the in-plane TMD excitons. As discussed in the "Introduction" section, this cannot be achieved via plasmonic NPoM cavities, thereby highlighting the advantage of using 1D plasmonic NGs.

Photo-excited carriers in an intermediate coupling system

In KPFM-based study, the SPD can be obtained using the contact potential difference (CPD) between the probe and samples. In KPFM measurement, the increase and decrease in the SP indicates

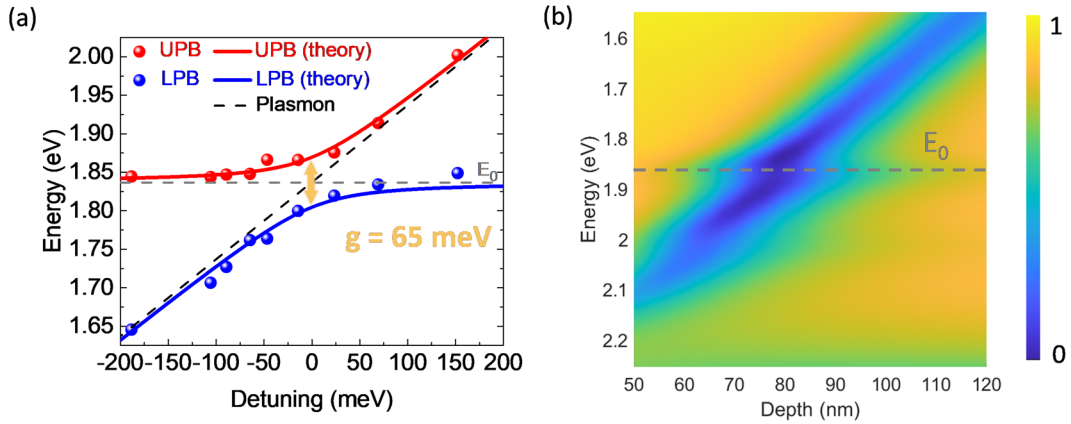

Fig. 3 Rabi splitting in hybrid systems of MoS_2 and Au NG arrays' hybrid system. a Dispersion of plexciton with UPB and LPB varied as functions of detuning. The dots correspond to the extract experimental data and the solid lines to the calculation results obtained using a coupled-oscillator model. The black dashed line represents the plasmon energy of the pure plasmonic cavity, and the gray dashed line indicates the excitons of the MoS_2 monolayers. The yellow arrow represents the Rabi splitting energy of this hybrid system, where the splitting energy is approximately 65 meV. **b** Simulated 2D contour plot of the reflectance for various NG depths. The gray dashed line represents the exciton resonance.

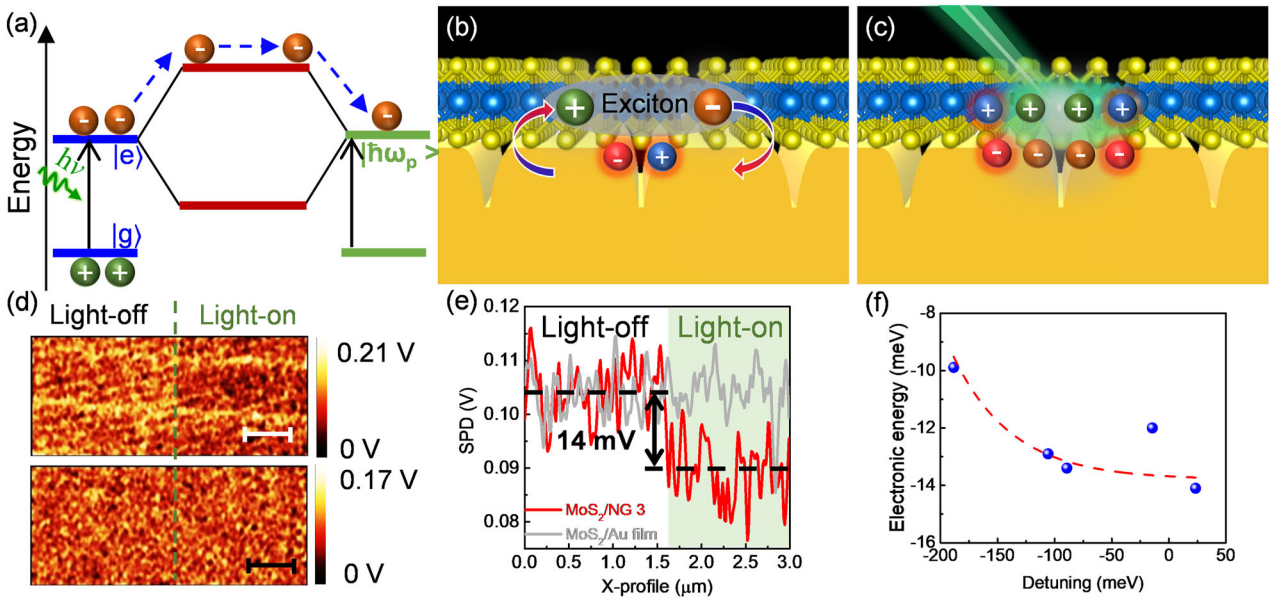

Fig. 4 SP change in intermediate coupling system. a Schematic illustration of photo-excited carriers' transfer process in intermediate coupling system. The illustration of electronic energy exchange in the intermediate coupling system with light-off (**b**) and light-on (**c**). **d** KPFM mapping image of MoS_2/NG3 (top panel) and MoS_2/Au film (bottom panel). The green dashed line indicates the place started illumination at 532 nm. The scale bars are 500 nm. **e** The SP profile of MoS_2/NG3 and MoS_2/Au films. These data were extracted from (**d**) and averaged for every column. The green marked area indicates the 532 nm light illumination during the measurement. **f** The blue dots are the measured electronic energy of intermediate coupling system as a function of detuning correspond to KPFM results. The red dashed line is the exponential decay fitting curve.

the accumulation of electrons and holes. To further understand the electronic-energy transfer process that occurs upon photo-excited carriers in the exciton–polariton coupling system, KPFM-based studies can be a crucial evidence (see Fig. 4). The SPD was measured on the same NG arrays by tuning the 532 nm laser on and off during the scanning. Therefore, the SPD that occurred upon illumination with 532 nm light is written as

$$\mathrm{SPD} = \left(\mathrm{SP}_{\mathrm{probe}} - \mathrm{SP}_{\mathrm{light-on}}\right) - \left(\mathrm{SP}_{\mathrm{probe}} - \mathrm{SP}_{\mathrm{light-off}}\right) = \Delta\mathrm{SP}_{\mathrm{light-on}} - \Delta\mathrm{SP}_{\mathrm{light-off}}. \quad (3)$$

As a control, a MoS_2/Au film was measured in the same measurement conditions. Another interesting feature in strong-coupling system is that it occurs even in the absence of light. Therefore, we excited MoS_2 exciton to observe carriers' transfer in the intermediate coupling system. Figure 4a illustrates the electronic energy transfer process. While the photon energy is greater than MoS_2 monolayers bandgap, the electron can be moved into the excited state and transferred to Au NG through the Rabi splitting channel. Figure 4d depicts the SP mapping of MoS_2/NG3 and MoS_2/Au film, the 532 nm laser is turned on at the position where labeled. The SP profiles were obtained by extracting the SP mapping of the average column. Clearly, the SP of MoS_2/NG3 decreased approximately 14 mV with the laser illumination. The SPD shows the trend as a function of detuning of the resonance in Fig. 4f. In the intermediate coupling regime, the localized electric field is induced by MoS_2 resonance which

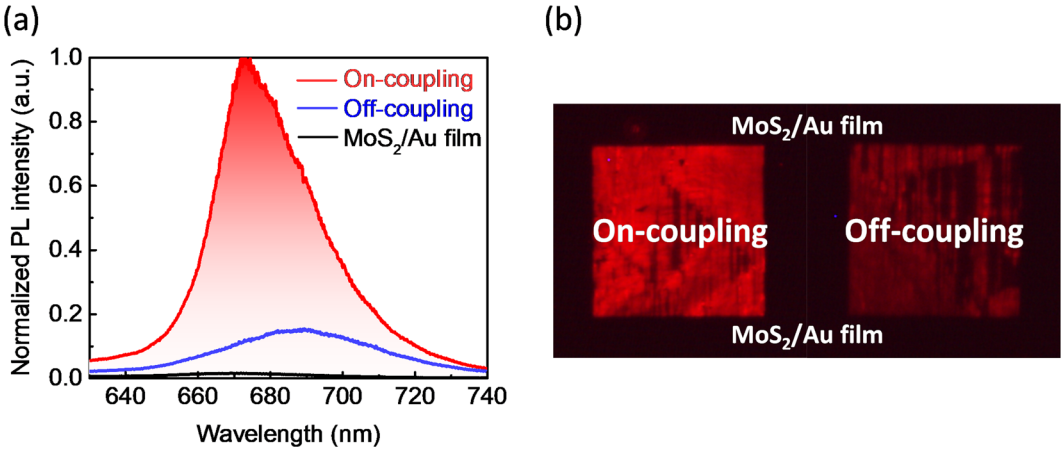

Fig. 5 PL properties of intermediate coupling systems. a Normalized PL spectra. **b** PL images of the MoS_2/Au films, on-coupling sample (MoS_2/NG3), and off-coupling sample (MoS_2/NG7), respectively.

Table 1. PL intensity and Purcell factor.

Sample	PL intensity (approximate values)	Purcell factor (approximate values)
MoS_2/Au film	1	3.57×10^2
MoS_2/NG7 off-coupling	10-fold	1.77×10^4
MoS_2/NG3 on-coupling	62-fold	4.03×10^4

indicates that the SPD is proportional to 1/detuning. However, the SP of MoS_2 on Au film did not respond to the laser illumination, because the thickness of MoS_2 monolayers is too thin and caused electron–hole pairs to accumulate at the MoS_2–Au interface, resulting in neutral SP. The quantitative calculation of electron densities in MoS_2 monolayers at various detuning levels are shown in Supplementary Fig. 4. At a detuning of ~23 meV, the electron density in MoS_2 is decreased to $3.22 \times 10^{12}\,cm^{-2}$, which can be attributed to MoS_2 carriers transferred to Au NGs. Therefore, it is clear that the measured SPD changes are induced by the intermediate coupling system.

PL enhanced via high Purcell factor

For the on-coupling sample (MoS_2/NG3), the excitons almost overlapped with the SPR, indicating significant PL enhancement, as depicted in Fig. 5. The plasmon-assisted PL-enhancement factor (EF) is determined as[37,38]

$$\mathrm{EF} = \left|\frac{E'}{E}\right|^2 \cdot \frac{\eta'}{\eta}, \tag{4}$$

where E and η denote the electric-field intensity and quantum yield, respectively, and the symbol with and without the "single-prime" represent with and without Au NG, respectively. The MoS_2 spontaneous emission rate of excitons in the hybrid system will be significantly fast because the SPR results in new radiative pathways. According to the Fermi's golden rule, the transition rate is proportional to the photonic density of states. Therefore, the PL EF can be simplified as

$$\mathrm{EF} \propto F_P \tag{5}$$

Moreover, MoS_2 incorporated with plasmonic cavities can tailor the luminescence spectra in terms of emission-intensity enhancement, peak position, and shape modification as also shown in Table 1, three of which have been widely studied[39–41]. When strong coupling occurs, the exciton–plasmon energy-exchange rate is higher than the radiative and non-radiative rates of excitons. Conversely, the energy is transferred from excitons to plasmons, and the excitons are then re-excited via the collective electron oscillation of plasmons in a strongly localized electric field. To characterize the relation between intermediate coupling and PL, the Purcell-factor calculations of on-coupling and off-coupling samples are listed in Table 1. The on-coupling sample with a high Purcell factor has high electromagnetic-field-confinement ability, which can assist in modifying the PL intensity and lifetime. Our demonstration of the photo-excited carriers in the intermediate coupling with MoS_2 monolayers on the proposed plasmonic metasurfaces was demonstrated only by photo-excitation. Since optically induced exciton–polariton coupling happens at the sub-100 femtosecond[28], our finding suggests the promising future of ultrafast plasmonic switches, by integrating 2D material with proposed plasmonic metasurfaces.

We successfully demonstrated that MoS_2 monolayers on top of 1D plasmonic NGs could achieve intermediate coupling at room temperature. The key feature of our structure was that the plasmonic fields and excitons were in parallel. The anticrossing curve revealed the Rabi splitting energy was approximately 65 meV, which is comparable with the excitonic linewidth but smaller than plasmon linewidth, confirming the intermediate coupling. The SP change that occurred upon photo-excited carriers' rearrangement was attributed to MoS_2 bandgap excitation and the induced hot-electron (hole) in Au NG. The observation of electronic energy exchange versus detuning of the plasmon resonance provides the evidence that the electronic equilibrium breaking via photo-excitation in the intermediate coupling system. The intermediate coupling phenomenon can also modify the PL intensity of the excitons. All the results confirmed that TMD-loaded 1D plasmonic NGs are ideal platforms to study the exciton–plasmon interaction. The findings of this study could initiate the development of various optoelectronic applications, such as low-threshold lasers and integrated plexciton devices. This work can provide a great potential for improving the performance of metal-2D semiconductor heterodevices in the field involving photoconversion.

METHODS

Growth and transfer of MoS_2-monolayer film

We performed salt-assisted CVD[29,30] to synthesize a monolayer MoS_2 film. First, 2 mg/ml aqueous solution of Na_2MoO_4 ($T_m = 687$ °C) was spin-coated on a sapphire substrate. Subsequently, the substrate was loaded in the center of the CVD chamber (a quartz tube; length: 1 m; diameter: 2 in). Approximately 100 mg of sulfur was loaded in the upstream of the

chamber. After sealing, the CVD chamber was pumped to approximately 1 Pa and restored to atmospheric pressure using 200 sccm high-purity argon. The furnace was heated at a ramp rate of 25 °C/min. The optimized growth condition for MoS_2 was 725–775 °C for approximately 5 min. For the transfer, a sapphire substrate with as-grown MoS_2 film was spin-coated with a layer of PMMA. Subsequently, the MoS_2/PMMA film was peeled from the sapphire substrate in DI water and transferred onto the target substrate. Notably, the PMMA layer can also be removed by sequentially rinsing in acetone and IPA.

Fabrication of Au NG arrays

First, 150-nm-thick gold films were deposited on silicon substrates using an electron-gun evaporation system. The NGs were then milled using a focused-ion-beam system (DB-FIB, FEI Helios NanoLab G3 CX, NCKU, Taiwan) under the acceleration voltage of 30 kV and ion beam current of 24 pA. The depths of the NGs were precisely controlled via dose adjustment.

Optical measurement

A confocal microscope (WITec Alpha 300S, Ulm, Germany) with a halogen lamp was used to measure the reflectance of the Au NGs. A 20× objective lens (Olympus) with a numerical aperture (NA) of 0.25 was used to collect the reflectance signal, which was recorded using a spectrometer (Acton SP2300, Princeton Instruments).

In Raman-spectroscopy and PL measurements, the samples were excited using a 532 nm Nd:YAG CW laser at 0.8 mW to avoid sample damage. The Raman and PL signals were investigated using a 50× objective lens (Olympus, MPlanFL) with an NA of 0.8. Additionally, a 532 nm notch filter was used to block the excited signal, which was resolved using a 600 g/mm diffraction grating and recorded using a spectrometer (Acton SP2300, Princeton Instruments).

KPFM measurement

The sample was mounted on an apparatus stage and electrically contacted to the ground. The SP difference was observed via KPFM using an atomic force microscope (TT-2, AFM Workshop) with SP measurement (SPT-20, Toyo Corporation). The probe was equipped with a Pt-coated tip at a frequency of approximately 70 kHz in the non-contact mode. In the SPT-20 setting, the alternating current bias, V_{ac}, applied 1 V at a frequency of 39 kHz to the probe.

Simulation

The FDTD method was employed to calculate the reflectance spectra, electric-field distribution, and Purcell factor by using a simulation software from Lumerical. In this modeling, the shapes of the Au NGs are same as the SEM cross-section images and were placed on the silicon substrate. The MoS_2 monolayers were then placed on top of the Au NGs, and the thickness of each monolayer was 0.6 nm. The wavelength-dependent refractive indices of Au and monolayer MoS_2 were as given in Johnson and Christy[42] and Jung et al.[43], respectively. Notably, *x*-polarized plane waves were used to illuminate the Au NGs and MoS_2/Au systems. In Purcell-factor calculation, an *x*-polarized dipole source was placed at the center of the MoS_2 monolayers to obtain the Purcell factor.

DATA AVAILABILITY

The data supporting the findings of this work are available from the corresponding author upon reasonable request.

Received: 30 November 2020; Accepted: 27 March 2021;
Published online: 23 April 2021

REFERENCES

1. McKeever, J., Boca, A., Boozer, A. D., Buck, J. R. & Kimble, H. J. Experimental realization of a one-atom laser in the regime of strong coupling. *Nature* **425**, 268–271 (2003).
2. Wu, S. et al. Monolayer semiconductor nanocavity lasers with ultralow thresholds. *Nature* **520**, 69–72 (2015).
3. Kasprzak, J. et al. Bose–Einstein condensation of exciton polaritons. *Nature* **443**, 409–414 (2006).
4. Deng, H., Weihs, G., Santori, C., Bloch, J. & Yamamoto, Y. Condensation of semiconductor microcavity exciton polaritons. *Science* **298**, 199–202 (2002).
5. Amo, A. et al. Superfluidity of polaritons in semiconductor microcavities. *Nat. Phys.* **5**, 805–810 (2009).
6. Baumann, K., Guerlin, C., Brennecke, F. & Esslinger, T. Dicke quantum phase transition with a superfluid gas in an optical cavity. *Nature* **464**, 1301–1306 (2010).
7. Törmä, P. & Barnes, W. L. Strong coupling between surface plasmon polaritons and emitters: a review. *Rep. Prog. Phys.* **78**, 013901 (2014).
8. Zengin, G. et al. Realizing strong light–matter interactions between single-nanoparticle plasmons and molecular excitons at ambient conditions. *Phys. Rev. Lett.* **114**, 157401 (2015).
9. Sun, J. et al. Light-emitting plexciton: exploiting plasmon–exciton interaction in the intermediate coupling regime. *ACS Nano* **12**, 10393–10402 (2018).
10. Vasa, P. et al. Real-time observation of ultrafast Rabi oscillations between excitons and plasmons in metal nanostructures with J-aggregates. *Nat. Photon.* **7**, 128 (2013).
11. Chikkaraddy, R. et al. Single-molecule strong coupling at room temperature in plasmonic nanocavities. *Nature* **535**, 127–130 (2016).
12. Stranius, K., Hertzog, M. & Börjesson, K. Selective manipulation of electronically excited states through strong light–matter interactions. *Nat. Commun.* **9**, 1–7 (2018).
13. Leng, H., Szychowski, B., Daniel, M.-C. & Pelton, M. Strong coupling and induced transparency at room temperature with single quantum dots and gap plasmons. *Nat. Commun.* **9**, 1–7 (2018).
14. Santhosh, K., Bitton, O., Chuntonov, L. & Haran, G. Vacuum Rabi splitting in a plasmonic cavity at the single quantum emitter limit. *Nat. Commun.* **7**, 1–5 (2016).
15. Wang, H. et al. Dynamics of strong coupling between CdSe quantum dots and surface plasmon polaritons in subwavelength hole array. *J. Phys. Chem. Lett.* **7**, 4648–4654 (2016).
16. Splendiani, A. et al. Emerging photoluminescence in monolayer MoS_2. *Nano Lett.* **10**, 1271–1275 (2010).
17. Mak, K. F., Lee, C., Hone, J., Shan, J. & Heinz, T. F. Atomically thin MoS_2: a new direct-gap semiconductor. *Phys. Rev. Lett.* **105**, 136805 (2010).
18. Park, S. et al. Direct determination of monolayer MoS_2 and WSe2 exciton binding energies on insulating and metallic substrates. *2D Mater.* **5**, 025003 (2018).
19. Xiao, J., Zhao, M., Wang, Y. & Zhang, X. Excitons in atomically thin 2D semiconductors and their applications. *Nanophotonics* **6**, 1309–1328 (2017).
20. Zhang, L., Gogna, R., Burg, W., Tutuc, E. & Deng, H. Photonic-crystal exciton–polaritons in monolayer semiconductors. *Nat. Commun.* **9**, 1–8 (2018).
21. Liu, X. et al. Strong light–matter coupling in two-dimensional atomic crystals. *Nat. Photon.* **9**, 30 (2015).
22. Wang, S. et al. Coherent coupling of WS2 monolayers with metallic photonic nanostructures at room temperature. *Nano Lett.* **16**, 4368–4374 (2016).
23. Kleemann, M.-E. et al. Strong-coupling of WSe 2 in ultra-compact plasmonic nanocavities at room temperature. *Nat. Commun.* **8**, 1–7 (2017).
24. Han, X., Wang, K., Xing, X., Wang, M. & Lu, P. Rabi splitting in a plasmonic nanocavity coupled to a WS2 monolayer at room temperature. *ACS Photon.* **5**, 3970–3976 (2018).
25. Schuller, J. A. et al. Orientation of luminescent excitons in layered nanomaterials. *Nat. Nanotechnol.* **8**, 271–276 (2013).
26. Hutchison, J. A. et al. Tuning the work-function via strong coupling. *Adv. Mater.* **25**, 2481–2485 (2013).
27. Shan, H. et al. Direct observation of ultrafast plasmonic hot electron transfer in the strong coupling regime. *Light Sci. Appl.* **8**, 1–9 (2019).
28. Du, W. et al. Ultrafast modulation of exciton–plasmon coupling in a monolayer WS2–Ag nanodisk hybrid system. *ACS Photon.* **6**, 2832–2840 (2019).
29. Li, S. et al. Wafer-scale and deterministic patterned growth of monolayer MoS_2 via vapor–liquid–solid method. *Nanoscale* **11**, 16122–16129 (2019).
30. Li, S. et al. Vapour–liquid–solid growth of monolayer MoS_2 nanoribbons. *Nat. Mater.* **17**, 535–542 (2018).
31. Li, H. et al. From bulk to monolayer MoS_2: evolution of Raman scattering. *Adv. Funct. Mater.* **22**, 1385–1390 (2012).
32. Wang, T. et al. Layer-number-dependent exciton recombination behaviors of MoS_2 determined by fluorescence-lifetime imaging microscopy. *J. Phys. Chem. C* **122**, 18651–18658 (2018).
33. Kim, K. S. et al. Atomic layer etching mechanism of MoS_2 for nanodevices. *ACS Appl. Mater. Interfaces* **9**, 11967–11976 (2017).
34. Wang, C.-Y. et al. Giant colloidal silver crystals for low-loss linear and nonlinear plasmonics. *Nat. Commun.* **6**, 7734 (2015).

35. Yu, M.-W. et al. Graphene-loaded plasmonic zirconium nitride and gold nanogroove arrays for surface charge modifications.*ACS Appl. Nano Mater.* **3**, 5002–5007 (2020).
36. Liu, W. et al. Strong exciton–plasmon coupling in MoS_2 coupled with plasmonic lattice. *Nano Lett.* **16**, 1262–1269 (2016).
37. Sriram, P. et al. Hybridizing strong quadrupole gap plasmons using optimized nanoantennas with bilayer MoS_2 for excellent photo-electrochemical hydrogen evolution. *Adv. Energy Mater.* **8**, 1801184 (2018).
38. Zhao, W. et al. Exciton–plasmon coupling and electromagnetically induced transparency in monolayer semiconductors hybridized with Ag nanoparticles. *Adv. Mater.* **28**, 2709–2715 (2016).
39. Zeng, Y. et al. Highly enhanced photoluminescence of monolayer MoS_2 with self-assembled Au nanoparticle arrays. *Adv. Mater. Interfaces* **4**, 1700739 (2017).
40. Ni, P. et al. Gate-tunable emission of exciton–plasmon polaritons in hybrid MoS_2-gap-mode metasurfaces. *ACS Photon.* **6**, 1594–1601 (2019).
41. Huang, J., Akselrod, G. M., Ming, T., Kong, J. & Mikkelsen, M. H. Tailored emission spectrum of 2D semiconductors using plasmonic nanocavities. *ACS Photon.* **5**, 552–558 (2018).
42. Johnson, P. B. & Christy, R.-W. Optical constants of the noble metals. *Phys. Rev. B* **6**, 4370 (1972).
43. Jung, G.-H., Yoo, S. & Park, Q.-H. Measuring the optical permittivity of two-dimensional materials without a priori knowledge of electronic transitions. *Nanophotonics* **8**, 263–270 (2018).

ACKNOWLEDGEMENTS

This work is partially supported by JSPS KAKENHI Grant Numbers 16H06364, 17H04801, and 19H02434, Japan. This work is also supported by the Higher Education Sprout Project of the National Chiao Tung University and Ministry of Education and the Ministry of Science and Technology (MOST 107-2221-E-009-046-MY3; 108-2218-E-009-031; 108-2923-E-009-003-MY3; 109-2628-E-009-007-MY3; 110-2923-E-009 -005 -MY2). M.-W.Y. would like to thank the Pilot Overseas Internships sponsored by the Ministry of Education, Taiwan and National Chiao Tung University, Taiwan. The authors would like to thank the Core Facility Center (CFC), National Cheng Kung University and Taiwan Semiconductor Research Institute (TSRI) for sample fabrication and the discussion with Dr. Chih-Chien Lin. Authors would also appreciate Mei-Lan Liang and Yen-Ju Wang's assistance in fabricating Au nanogrooves with FIB. The authors would acknowledge the fruitful discussion with Prof. Tien-Chang Lu and Prof. Shiuan-Yeh Chen.

AUTHOR CONTRIBUTIONS

M.-W.Y., S.I., and K.-P.C. initiated the work. S.-L. grew and transferred MoS_2. M.-W.Y, J.-R.K., and K.-L.S. fabricated Au NG arrays. M.-W.Y. performed the numerical simulation and modeling. M.-W.Y., J.-R.K., J.-H.Y, S.L., and T.T. performed the optical experiment. M.-W.Y. performed the KPFM measurements. M.-W.Y., S.I., T.N., and K.-P.C. analyzed the experiment data. M.-W. Y., S.I., and K.-P.C. wrote the manuscript. All the authors discussed the results and commented on the manuscript.

COMPETING INTERESTS

The authors declare no competing interests.

ADDITIONAL INFORMATION

Supplementary information The online version contains supplementary material available at https://doi.org/10.1038/s41699-021-00227-y.

Correspondence and requests for materials should be addressed to S.I. or K.-P.C.

Reprints and permission information is available at http://www.nature.com/reprints

Publisher's note Springer Nature remains neutral with regard to jurisdictional claims in published maps and institutional affiliations.